Front. Struct. Civ. Eng. 2022, 16(9): 1089–1103
https://doi.org/10.1007/s11709-022-0851-z

RESEARCH ARTICLE

A multi-objective design method for seismic retrofitting of existing reinforced concrete frames using pin-supported rocking walls

Yue CHEN[a,b,c], Rong XU[b], Hao WU[a,c*], Tao SHENG[d]

[a] *Institute of Engineering Mechanics, China Earthquake Administration; Key Laboratory of Earthquake Engineering and Engineering Vibration of China Earthquake Administration, Harbin 150088, China*

[b] *Research Center of Industrialization Construction Technology of Zhejiang Province, Ningbo University of Technology, Ningbo 315106, China*

[c] *State Key Laboratory of Disaster Reduction in Civil Engineering, Tongji University, Shanghai 200092, China*

[d] *College of Civil and Environmental Engineering, Ningbo University, Ningbo 315211, China*

[*] *Corresponding author. E-mail: 2009wuhao_tom@tongji.edu.cn*

ABSTRACT Over the past several decades, a variety of technical ways have been developed in seismic retrofitting of existing reinforced concrete frames (RFs). Among them, pin-supported rocking walls (PWs) have received much attentions to researchers recently. However, it is still a challenge that how to determine the stiffness demand of PWs and assign the value of the drift concentration factor (*DCF*) for entire systems rationally and efficiently. In this paper, a design method has been exploited for seismic retrofitting of existing RFs using PWs (RF-PWs) via a multi-objective evolutionary algorithm. Then, the method has been investigated and verified through a practical project. Finally, a parametric analysis was executed to exhibit the strengths and working mechanism of the multi-objective design method. To sum up, the findings of this investigation show that the method furnished in this paper is feasible, functional and can provide adequate information for determining the stiffness demand and the value of the *DCF* for PWs. Furthermore, it can be applied for the preliminary design of these kinds of structures.

KEYWORDS pin-supported rocking wall, reinforced concrete frame, seismic retrofit, stiffness demand, drift concentration factor, multi-objective design, genetic algorithm, Pareto optimal solution

1 Introduction

In the last few decades, reinforced concrete frames (RFs) have been utilized widely in seismic areas all over the world. It is well-known that an RF should possess enough energy dissipation capacity and ductility in order to reduce seismic responses [1,2]. Consequently, it often causes large residual drifts and momentous structural damage under severe seismic excitations. On account of this, severe economic losses will be incurred and rebuilding or repairing necessities will be needed after a serious earthquake. Furthermore, the idea of "Strong Column Weak Beam" has been adopted in leading seismic design codes in many countries for several decades [3]. However, weak-story failures and inter-story drift concentrations have emerged in some high-rise frames designed on the basis of the existing codes. Besides, many existing RFs have structural deficiencies owing to the inadequacy of old design provisions, e.g., some regions with high seismic risks now were not diagnosed as they are or their levels of seismic hazards were underestimated before the upgraded codes [4].

In the light of the reasons depicted above, the seismic retrofitting of existing RFs is considered to be increasingly drawing the attention in earthquake engineering field currently. Numerous techniques have been

Article history: Received Nov 8, 2021; Accepted Apr 15, 2022

developed for seismic retrofitting of existing RFs and can be employed in combination or alternatively to improve the seismic performance of structures, such as: Buckling Restrained Braces (BRBs) [5–9], Fiber-Reinforced Polymer (FRP) [4,10], Base Isolation [11–17], Precast concrete spreader-wall [18], Dissipative steel exoskeletons [19] and reinforced concrete rocking walls [1,20–24], etc.

Among them, RC rocking walls have been exploited to mitigate the seismic vulnerability of existing structures in the last decade [21,25]. Generally speaking, reinforced concrete rocking walls can be classified into two categories, viz. pin-supported and stepping rocking walls (see Fig. 1). Their major difference is that the former rocks around only one fulcrum, while the latter has fulcrums on both sides of the bottom of the rocking wall [26]. In this paper, the pin-supported rocking walls (PWs) is concentrated on and investigated both conceptually and theoretically.

Moreover, the existing body of research on retrofitting of existing RFs via PWs suggests that the deformation pattern of RFs can be controlled effectively using PWs so as to avoid weak story failures and inter-story drift concentrations [1,27]. The effectiveness of PWs in reducing inter-story drift concentrations can be indicated viz. the drift concentration factor (*DCF*) [1,21], i.e., *DCF* can be employed to assess the uniformity of Inter-Drift Ratios (*IDR*s) of structures. The expression of *DCF* can be defined as Eq. (1).

$$DCF = \frac{\max\limits_i \dfrac{d_i}{h_i}}{\Delta / \sum_i h_i}, \tag{1}$$

where d_i, h_i, and Δ mean the inter-story displacement, the story height, and the roof displacement of structures, respectively. Specifically, the closer to 1.0 the value of *DCF* is, the better deformation pattern of the structure is controlled. However, a uniform *DCF* would be an ideal case while it would demand an impractical and infinite PW. Furthermore, a major problem in applying *DCF* to reflect PW's effect, which has been found in most previous research with regard to the stiffness demand, is difficult to assign a design target value, i.e., the determination of the *DCF* is blind and its physical meaning would be obscure. Therefore, it is worth studying that how to choose the appropriate *DCF* value in the light of the actual engineering requirements and structural performance demands.

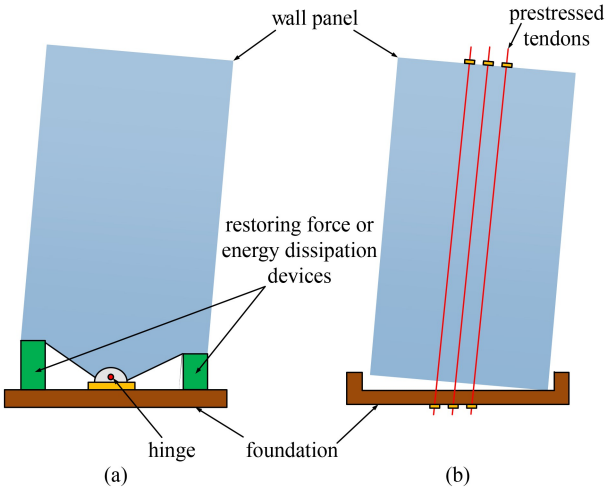

Fig. 1 Reinforced concrete rocking walls: (a) pin-supported rocking wall; (b) stepping rocking wall.

In this study, a design method by a multi-objective evolutionary optimization (MEO) is explored for seismic retrofitting of existing RFs using PWs (RF-PWs). Specifically, based on genetic algorithm (GA) and the theories of RFs retrofitted with PWs, a group of Pareto Optimal Solutions (POSs) will be furnished, which not only meets the performance requirements of the retrofitted structures but also possesses a characteristic of diversity. Meantime, the physical meaning of *DCF*s and the performance of the retrofitted structures can be displayed clearly and intuitively. Afterwards, the best one can be selected by designers through comparing the differences of individuals in the POSs. The multi-objective design method may boost the preliminary design of this kind of structures.

2 Multi-objective evolutionary optimization via genetic algorithm

It is well-known that MEO methods have been the significant techniques to tackle practical problems in the last decade [28]. In engineering fields, most real-world problems get involved in optimizing multi-objectives simultaneously which have tradeoff relationship normally. In general, the commonly used form of the MEO problem can be stated as Eq. (2).

$$\left.\begin{aligned} \text{Minimize/maximize} \quad & F_m(z),\ m = 1,2,\ldots,M; \\ & G_j(z) \geqslant 0,\ j = 1,2,\ldots,J; \\ \text{subject to} \quad & H_k(z) = 0,\ k = 1,2,\ldots,K; \\ & C_r(z) \leqslant 0,\ r = 1,2,\ldots,R; \\ & D_s(z) = 0,\ s = 1,2,\ldots,S; \\ & z_{(l)i} \leqslant z_i \leqslant z_{(u)i},\ i = 1,2,\ldots,n. \end{aligned}\right\}, \tag{2}$$

where z is the design variables' vector: $z = (z_1, z_2, \ldots, z_n)^{\mathrm{T}}$; $F_m(z)$ is the objective functions' vector: $F_m(z) = (f_1(z), f_2(z), \ldots, f_M(z))^{\mathrm{T}}$; $G_j(z)$ means the constraints' vector of linear inequality: $G_j(z) = (g_1(z), g_2(z), \ldots, g_J(z))^{\mathrm{T}}$; $H_k(z)$ denotes the constraints' vector of linear equality: $H_k(z) = (h_1(z), h_2(z), \ldots, h_K(z))^{\mathrm{T}}$; $C_r(z)$ stands for the constraints' vector of nonlinear inequality: $C_r(z) = (c_1(z), c_2(z), \ldots, c_R(z))^{\mathrm{T}}$; $D_s(z)$ symbolizes the constraints' vector of nonlinear equality: $D_s(z) = (d_1(z), d_2(z), \ldots, d_S(z))^{\mathrm{T}}$;

$z_{(l)i}$, $z_{(u)i}$ represent the lower and upper bounds on z_i, respectively.

In this study, GA was suggested to address this problem [29,30]. Meantime, the schematic of the EMO using GA is presented in Fig. 2.

Moreover, NSGA-II approach in which ranking is based sequentially on: (1) constraint satisfaction, (2) domination, and (3) crowding distance was utilized to address the multiobjective optimization [31,32]. The EMO using GA was executed through the GA Optimization Toolbox in Matlab [33]. Table 1 shows the parameters adopted by EMO using GA in this study.

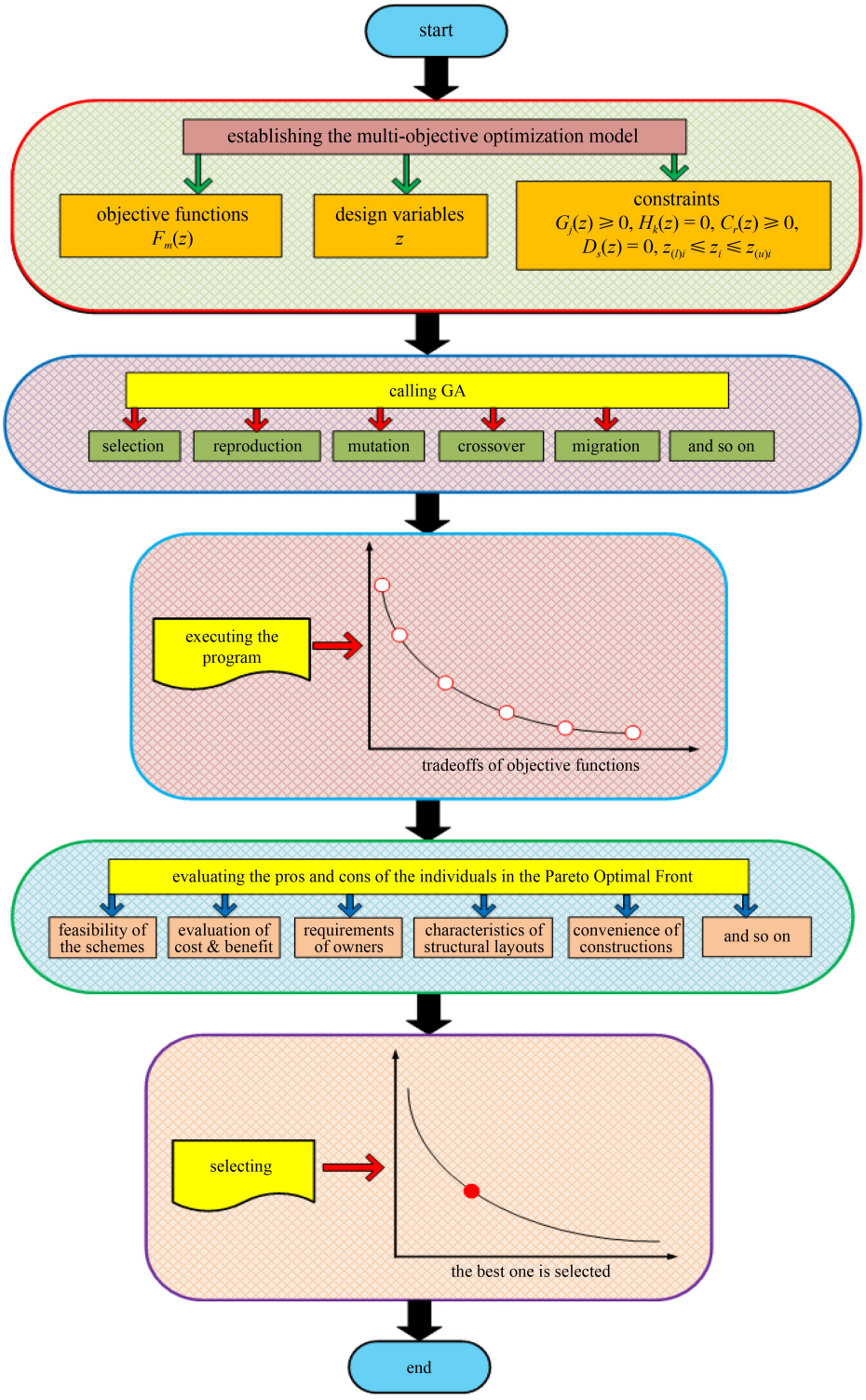

Fig. 2 Schematic of the EMO using GA.

Table 1 Parameters adopted by EMO using GA

parameter	value
type of population	double vector
size of population	100
selection	tournament
size of tournament	2
reproduction	0.8
mutation	constraint dependent
ratio of crossover	1.0
measure of distance	@distancecrowding
fraction of Pareto front population	0.5
stopping criteria	50

3 Parametric model for seismic retrofitting of existing reinforced concrete frames using pin-supported rocking walls

In this study, the model for RF-PWs is displayed in Fig. 3. Figures 3(a)–3(e) represent the lateral load, RF, PW with a rotational spring, RF-PW and parametric model for RF-PWs, respectively. Specifically, the RF-PW is simulated as a combination of and one flexural beam one shear beam linked with rigid links at the location of the floors (see Fig. 3(e)). The flexural beam and the shear beam symbolize the PW and the RF, respectively.

In Fig. 3(e), $p(x)$ is the lateral load, which is assigned along the structure's height whereas $p_F(x)$ represents the distributed internal force between the RF and the PW, where x means the height from the bottom to a certain position of the structure; H stands for the entire structure's height; E_wI_w is the bending stiffness of the PW; K with a unit of Newtons denotes the shear distributed stiffness of the RF, which equals the shear force when a unit *IDR* is applied. K_r is the rotational spring's stiffness on the bottom of the PW [26,34,35].

According to the Refs. [26,34], the differential equations and the corresponding solutions can be derived (see Tables 2 and 3) under four different lateral load models. Accordingly, the bending moment M_w and shear force V_w of the flexural beam can be obtained as Eqs. (3) and (4), respectively.

$$M_w = \frac{E_wI_w}{H^2}\frac{d^2y}{d\xi^2}, \tag{3}$$

$$V_w = -\frac{E_wI_w}{H^3}\frac{d^3y}{d\xi^3}. \tag{4}$$

4 Case study

4.1 Model of multi-objective evolutionary optimization via genetic algorithm

The problem of an RF-PW can be stated as follows:

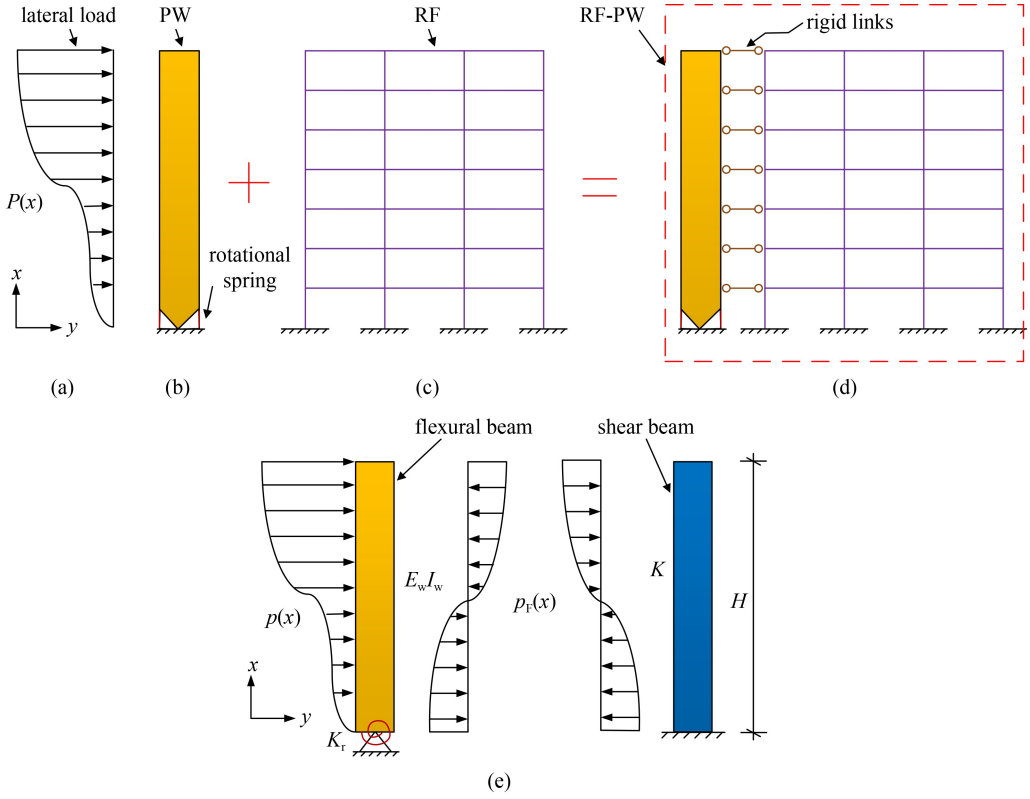

Fig. 3 Model for RF-PWs: (a) lateral load; (b) PW with a rotational spring; (c) RF; (d) RF-PW; (e) parametric model of RF-PWs.

Table 2 Expressions of $y(\xi)$ corresponding to the four different $p(\xi)$

$p(\xi)$	differential equations	solutions of differential equations	boundary conditions
q	$-\lambda^2\frac{\mathrm{d}^2y}{\mathrm{d}\xi^2}=\frac{qH^4}{E_wI_w}$	$y(\xi)=C_1+C_2\xi+A\sinh\lambda\xi+B\cosh\lambda\xi-\frac{qH^2}{2K}\xi^2$	(1) When $x=H,(\xi=1)$, Shear blance, $\left(\frac{\mathrm{d}^3y}{\mathrm{d}\xi^3}-\lambda^2\frac{\mathrm{dy}}{\mathrm{d}\xi}\right)_{\xi=1}=0.$
$q\cdot\xi$	$-\lambda^2\frac{\mathrm{d}^2y}{\mathrm{d}\xi^2}=\frac{q\xi H^4}{E_wI_w}$	$y(\xi)=C_1+C_2\xi+A\sinh\lambda\xi+B\cosh\lambda\xi+\frac{qH^2}{6K}\xi^3$	(2) When $x=0,(\xi=0)$, Moment balance, $\left(R_\mathrm{f}\frac{\mathrm{dy}}{\mathrm{d}\xi}-\frac{\mathrm{d}^2y}{\mathrm{d}\xi^2}\right)_{\xi=0}=0.$
$q\cdot\sqrt{\xi}$	$-\lambda^2\frac{\mathrm{d}^2y}{\mathrm{d}\xi^2}=\frac{q\sqrt{\xi}H^4}{E_wI_w}$	$y(\xi)=C_1+C_2\xi+A\sinh\lambda\xi+B\cosh\lambda\xi+\frac{4qH^2}{15K}\xi^{\frac{5}{2}}$	(3) When $x=0,(\xi=0)$, $y=0$, $y_{\xi=0}=0$.
F	$\frac{\mathrm{d}^4y}{\mathrm{d}\xi^4}=\lambda^2\frac{\mathrm{d}^2y}{\mathrm{d}\xi^2}$	$y(\xi)=C_1+C_2\xi+A\sinh\lambda\xi+B\cosh\lambda\xi$	(4) When $x=H,(\xi=1)$, $\left(\frac{\mathrm{d}^2y}{\mathrm{d}\xi^2}\right)_{\xi=1}=0.$

Notes: $y(\xi)$ is the lateral displacement along the structure's height; $p(\xi)$ is the lateral load acting on the structure; ξ is the dimensionless height, $\xi=\frac{x}{H}$ and $0\leqslant\xi\leqslant1.0$; λ means the ratio of the stiffness between the shear beam and the flexural beam, $\lambda=H\sqrt{\frac{K}{E_\mathrm{w}I_\mathrm{w}}}$; R_f denotes the normalized rotational spring stiffness, $R_\mathrm{f}=\frac{K_\mathrm{r}H}{E_\mathrm{w}I_\mathrm{w}}$ and $0\leqslant R_\mathrm{f}<\infty$; C_1, C_2, A and B are the unknown coefficients of the solutions of the differential equations, respectively (see Table 3); F means a concentrated load at the top of the structure.

Table 3 Solutions of C_1, C_2, A and B

coefficients	uniformly distributed load	inverted triangular distributed load	parabolic distributed load	concentrated load at the top of the structure
φ	$\frac{1-\cosh\lambda-R_\mathrm{f}\cosh\lambda}{\sinh\lambda+\frac{R_\mathrm{f}}{\lambda}\cosh\lambda}$	$\frac{1-R_\mathrm{f}\left(\frac{1}{2}-\frac{1}{\lambda^2}\right)\cosh\lambda}{\sinh\lambda+\frac{R_\mathrm{f}}{\lambda}\cosh\lambda}$	$\frac{1-R_\mathrm{f}\left(\frac{2}{3}-\frac{1}{2\lambda^2}\right)\cosh\lambda}{\sinh\lambda+\frac{R_\mathrm{f}}{\lambda}\cosh\lambda}$	$\frac{R_\mathrm{f}\cosh\lambda}{\sinh\lambda+\frac{R_\mathrm{f}}{\lambda}\cosh\lambda}$
C_1	$-\frac{qH^2}{K\lambda^2}\left(1+R_\mathrm{f}+\frac{R_\mathrm{f}}{\lambda}\varphi\right)$	$-\frac{qH^2}{K\lambda^2}\left[\frac{R_\mathrm{f}}{\lambda^2}\left(\frac{1}{2}-\frac{1}{\lambda^2}\right)+\frac{R_\mathrm{f}}{\lambda}\varphi\right]$	$-\frac{qH^2}{K\lambda^2}\left[\frac{R_\mathrm{f}}{\lambda^2}\left(\frac{2}{3}-\frac{1}{2\lambda^2}\right)+\frac{R_\mathrm{a}}{\lambda}\varphi\right]$	$-\frac{FH}{K\lambda^2}\left(R_\mathrm{f}-\frac{R_\mathrm{f}}{\lambda}\varphi\right)$
C_2	$\frac{qH^2}{K}$	$\frac{qH^2}{K}\left(\frac{1}{2}-\frac{1}{\lambda^2}\right)$	$\frac{qH^2}{K}\left(\frac{2}{3}-\frac{1}{2\lambda^2}\right)$	$\frac{FH}{K}$
A	$\frac{qH^2}{K\lambda^2}\varphi$	$\frac{qH^2}{K\lambda^2}\varphi$	$\frac{qH^2}{K\lambda^2}\varphi$	$-\frac{FH^2}{K\lambda^2}\varphi$
B	$\frac{qH^2}{K\lambda^2}\left(1+R_\mathrm{f}+\frac{R_\mathrm{f}}{\lambda}\varphi\right)$	$\frac{qH^2}{K\lambda^2}\left[\frac{R_\mathrm{f}}{\lambda^2}\left(\frac{1}{2}-\frac{1}{\lambda^2}\right)+\frac{R_\mathrm{f}}{\lambda}\varphi\right]$	$\frac{qH^2}{K\lambda^2}\left[\frac{R_\mathrm{f}}{\lambda^2}\left(\frac{2}{3}-\frac{1}{2\lambda^2}\right)+\frac{R_\mathrm{f}}{\lambda}\varphi\right]$	$\frac{FH}{K\lambda^2}\left(R_\mathrm{f}-\frac{R_\mathrm{f}}{\lambda}\varphi\right)$

Notes: φ is a symbol to simplify the expressions of C_1, A and B.

One Design Variable:

Find

$E_\mathrm{w}I_\mathrm{w}=E_\mathrm{w}\cdot I_\mathrm{w}$,

where $E_\mathrm{w}I_\mathrm{w}$ is the bending stiffness of the cross-section of the PW; E_w is the elasticity modulus of concrete of the PW; I_w means the section moment of inertia of the PW, $I_\mathrm{w}=\frac{t_\mathrm{w}b_\mathrm{w}^3}{12}$; where t_w is the thickness of the PW (unit: m); b_w is the width of the PW (unit: m).

Two Trade-off Objective Functions:

(1) η and (2) DCF^PW,

where $\eta=\frac{1}{\lambda}\cdot\eta$, the reciprocal of λ, is a nondimensional parameter representing the stiffness ratio between the flexural beam and shear beam; and DCF^PW is the DCF of the PW.

Constraints:

Subjected to:

(1) the range of the design variable, $E_\mathrm{w}I_\mathrm{w}$.

$$1.0\times10^7\leqslant E_\mathrm{w}I_\mathrm{w}\leqslant1.0\times10^9,$$

where in order to determine the range of the design variable, $t_\mathrm{w}=0.6$ and $1.0\leqslant b_\mathrm{w}<9.0$ are assumed, respectively.

(2) the range of the maximum IDR of the RF-PW, $IDR_\mathrm{max}^\mathrm{PW}$.

$$0<IDR_\mathrm{max}^\mathrm{PW}<IDR_\mathrm{max}^\mathrm{RF}.$$

For the efficiency of convergence of the optimization program, the restraint of $IDR_\mathrm{max}^\mathrm{PW}$ is set between 0 and $IDR_\mathrm{max}^\mathrm{RF}$, where the $IDR_\mathrm{max}^\mathrm{RF}$ denotes the maximum IDR of the RF and equals 1/1289 in this case (see Table 5).

(3) the range of the DCF of the RF-PW, DCF^PW.

$$1.0<DCF^\mathrm{PW}<DCF^\mathrm{RF},$$

where the DCF^RF denotes the DCF of the RF and equals 1.62 in this case.

4.2 Case employed in this study

Figure 4 presents an existing two-dimensional five-story RF [26]. In this case, the bending stiffness of the frame beams is assumed to be infinite; $K=1.86\times10^6$ kN; the uniformly distributed load is adopted as the lateral load acting on the structure, i.e., $p(\xi)=q$, where $q=100$ kN/m; $K_r=0$, i.e., no rotational spring is set. Furthermore, the

basic information of the RF is given in Table 4.

It is very easy to obtain the lateral displacement and *IDR*s of the RF by any kind of finite element software. The lateral displacements and IDR^{RF} of the RF are furnished in Table 5 and Fig. 5, respectively. As shown in Table 5 and Fig. 5, the maximum lateral displacement and IDR^{RF}_{max} of the structure are 7.17 mm and 1/1289, respectively. Furthermore, the DCF^{RF} of the structure equals 1.62 according to Eq. (1), where IDR^{RF}_{max} and DCF^{RF} represent the maximum *IDR* and the *DCF* of the RF, respectively.

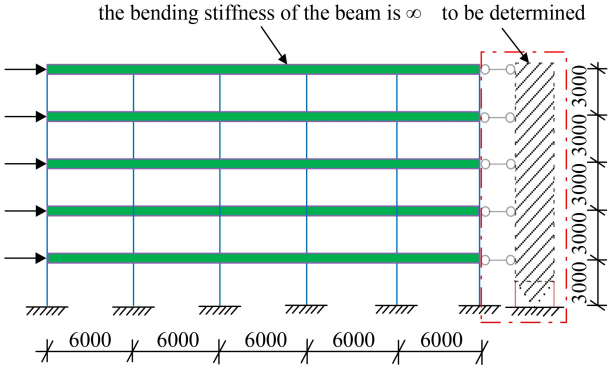

Fig. 4 Two-dimensional five-story RF before retrofitted.

Table 4 Material and geometrical dimensions of the RF

concrete	E_f (kN/m^2)	story number	story height (m)	span number	span (m)	columns' cross section (m^2)
C30	3.0×10^7	5	3.0	5	6.0	0.6×0.6

Note: E_f is the elasticity modulus of concrete for the RF.

Table 5 Lateral displacements and *IDR*s of the RF

position	lateral displacement (mm)	IDR^{RF}
roof	7.16577	1/5709
4th floor	6.64028	1/3045
3rd floor	5.65518	1/2083
2nd floor	4.21509	1/1588
1st floor	2.32695	1/1289
ground	0	–

Note: IDR^{RF} represents the *IDR* of the RF.

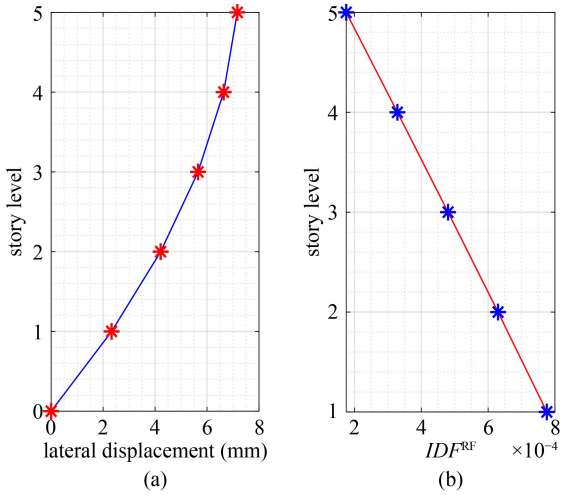

Fig. 5 (a) Lateral displacement and (b) *IDR* of the RF.

5 Results analysis

According to Table 1, the number of POSs will be 50 in this case, for Population size and Pareto front population fraction are 100 and 0.5, respectively. Table 6 provides the 50 individuals of POSs at Generation 50. Figures 6 and 7 show the bar diagrams of two objective functions, viz. η and *DCF*, of 50 POSs at Generation 50, respectively. From Table 6 and Figs. 6–7, we can see that $0.169 \leqslant \eta \leqslant 1.514$, and $1.026 \leqslant DCF^{PW} \leqslant 1.494$. It is apparent that the values of DCF^{PW} are all smaller than the one of DCF^{RF}, viz. 1.62 (the red bar in right side of Fig. 7), which means the effectiveness of the PW in reducing inter-story drift concentrations of the RF.

Figure 8 displays the scatter diagram between two objective functions, viz. η and DCF^{PW}, at Generation 50. Looking at Fig. 8, it is clear that a trade-off correlation is demonstrated between η and DCF^{PW}, i.e., specifically, with the gradual increase of η, DCF^{PW} will continue to decrease, and vice versa. i.e., with the rise of E_wI_w, the deformation control effect of the PW on the RF will be increasingly obvious.

Figures 9 and 10 present the 3D and plan diagrams of the quantity distribution of objective function values of 50 POSs at Generation 50. From Figs. 9 and 10, we can see that some values of the objective functions among POSs are very close, which can be considered as equal individuals. e.g., when $1.45 \leqslant DCF^{PW} < 1.5$, $0.17 \leqslant \eta < 0.31$ and $1.03 \leqslant DCF^{PW} < 1.07$, $1.38 \leqslant \eta < 1.52$, there are 6 and 4 similar POSs, respectively. In addition, as shown in Figs. 9 and 10, there are 18 kinds of POSs, which displays a relatively uniform scatter. Also, no local convergence appears. As a consequence, the solutions of multi-objective optimization have the characteristic of diversity in contrast to the only one of single objective optimization.

Figures 11 and 12 display the scatter and bar diagrams of the distribution of the design variables, viz. the bending stiffness of the PW, E_wI_w, of 50 POSs at Generation 50, respectively. Figure 13 presents the diagram of the relationship between b_w and DCF^{PW}. From Figs. 11 and 12, we can see that the distribution of the design variables has good discreteness and diversity. From Fig. 13, it is evident that there is an inverse correlation between b_w and DCF^{PW}. Moreover, the width of the PW, viz. b_w can be acquired when t_w is set as 0.6 m and $E_w = E_f$, respectively (see Fig. 14). It can be seen from Table 6 and Fig. 14 that $2.0\ \text{m} \leqslant b_w \leqslant 8.6\ \text{m}$, which means there are a variety of options when designers try to

Table 6 50 POSs at Generation 50

No.	η	DCF^{PW}	$E_wI_w \times 10^{-7}$ (kN·m^2)	b_w (m) / t_w = 0.6 m	λ	IDR_{max}^{PW}	ζ	V_{wb} (kN)	δ
1	0.311	1.321	4.058	3.0	3.211	1/1537	83.8%	430.5	25.9%
2	1.266	1.037	67.1	7.6	0.790	1/1958	65.8%	712.6	42.8%
3	1.514	1.026	96.0	8.6	0.660	1/1978	65.2%	723.2	43.4%
4	0.258	1.380	2.784	2.6	3.877	1/1472	87.6%	370.8	22.3%
5	0.188	1.469	1.472	2.1	5.332	1/1382	93.3%	278.4	16.7%
6	0.392	1.249	6.439	3.5	2.549	1/1626	79.3%	502.6	30.2%
7	0.331	1.301	4.592	3.1	3.019	1/1560	82.6%	450.1	27.0%
8	0.223	1.422	2.09	2.4	4.475	1/1428	90.3%	327.3	19.7%
9	0.758	1.094	24.0	5.4	1.319	1/1857	69.4%	656.6	39.4%
10	0.723	1.101	21.9	5.3	1.383	1/1844	69.9%	649.0	39.0%
11	1.197	1.041	60.0	7.4	0.835	1/1950	66.1%	708.5	42.6%
12	0.249	1.390	2.603	2.6	4.010	1/1461	88.2%	360.4	21.6%
13	0.531	1.165	11.8	4.3	1.883	1/1742	74.0%	585.6	35.2%
14	0.269	1.367	3.033	2.7	3.714	1/1486	86.7%	384.2	23.1%
15	0.169	1.494	1.2	2.0	5.905	1/1359	94.8%	252.4	15.2%
16	0.358	1.277	5.373	3.3	2.791	1/1591	81.0%	474.8	28.5%
17	1.120	1.047	52.5	7.0	0.892	1/1940	66.4%	703.2	42.2%
18	1.514	1.026	96.0	8.6	0.660	1/1978	65.2%	723.2	43.4%
19	0.657	1.119	18.1	4.9	1.522	1/1815	71.0%	631.7	37.9%
20	0.172	1.490	1.24	2.0	5.809	1/1363	94.6%	256.4	15.4%
21	0.484	1.189	9.812	4.0	2.065	1/1708	75.5%	562.3	33.8%
22	0.806	1.084	27.2	5.7	1.241	1/1873	68.8%	665.9	40.0%
23	1.040	1.054	45.3	6.7	0.962	1/1927	66.9%	696.4	41.8%
24	1.404	1.031	82.5	8.2	0.712	1/1970	65.4%	719.1	43.2%
25	0.293	1.340	3.599	2.9	3.410	1/1515	85.0%	411.3	24.7%
26	0.245	1.396	2.504	2.6	4.089	1/1455	88.6%	354.4	21.3%
27	0.196	1.458	1.61	2.2	5.098	1/1393	92.5%	290.4	17.4%
28	1.346	1.033	75.8	8.0	0.743	1/1966	65.6%	716.6	43.0%
29	1.346	1.033	75.8	8.0	0.743	1/1966	65.6%	716.6	43.0%
30	0.238	1.404	2.366	2.5	4.205	1/1446	89.1%	345.9	20.8%
31	1.467	1.028	90.1	8.4	0.681	1/1975	65.3%	721.5	43.3%
32	0.574	1.147	13.8	4.5	1.741	1/1770	72.8%	603.9	36.3%
33	0.475	1.194	9.423	4.0	2.107	1/1700	75.8%	556.9	33.4%
34	0.874	1.073	31.9	6.0	1.145	1/1892	68.1%	676.9	40.7%
35	0.806	1.084	27.2	5.7	1.241	1/1873	68.8%	665.9	40.0%
36	0.268	1.368	3.004	2.7	3.733	1/1484	86.8%	382.7	23.0%
37	0.289	1.345	3.488	2.9	3.464	1/1510	85.4%	406.3	24.4%
38	0.551	1.157	12.7	4.4	1.815	1/1756	73.4%	594.3	35.7%
39	0.180	1.479	1.361	2.1	5.545	1/1373	93.9%	268.2	16.1%
40	1.169	1.043	57.2	7.2	0.856	1/1947	66.2%	706.6	42.4%
41	0.429	1.222	7.715	3.7	2.329	1/1661	77.6%	529.2	31.8%
42	0.311	1.321	4.058	3.0	3.211	1/1537	83.8%	430.5	25.9%
43	0.612	1.133	15.7	4.7	1.634	1/1792	71.9%	617.6	37.1%
44	0.228	1.416	2.181	2.4	4.381	1/1434	89.9%	333.6	20.0%
45	1.273	1.037	67.8	7.7	0.786	1/1959	65.8%	713.0	42.8%

(*Continued*)

No.	η	DCF^{PW}	$E_wI_w \times 10^{-7}$ (kN·m^2)	b_w (m) / t_w = 0.6 m	λ	IDR_{max}^{PW}	ζ	V_{wb} (kN)	δ
46	0.948	1.063	37.6	6.3	1.055	1/1910	67.5%	686.7	41.2%
47	0.408	1.237	6.952	3.6	2.454	1/1641	78.5%	514.0	30.9%
48	0.210	1.439	1.854	2.3	4.751	1/1411	91.3%	310.0	18.6%
49	0.169	1.494	1.2	2.0	5.905	1/1359	94.8%	252.4	15.2%
50	0.331	1.301	4.592	3.1	3.019	1/1560	82.6%	450.1	27.0%

Notes: ζ is a nondimensional parameter, which represents the ratio between the maximum *IDR* of the RF-PW and the one of the RF, $\zeta = \dfrac{IDR_{max}^{PW}}{IDR_{max}^{RF}} \times 100\%$; V_{wb} is the shear force at the bottom of the flexural beam; δ is a nondimensional parameter, which means the ratio between the shear force at the bottom of the PW and the resultant force of the lateral load, $\delta = \dfrac{V_{wb}}{\int_0^1 p(\xi)\mathrm{d}\xi} \times 100\%$, e.g., if a uniformly distributed load, viz. $p(\xi) = q$, is employed, $\delta = \dfrac{V_{wb}}{q \cdot H} \times 100\%$.

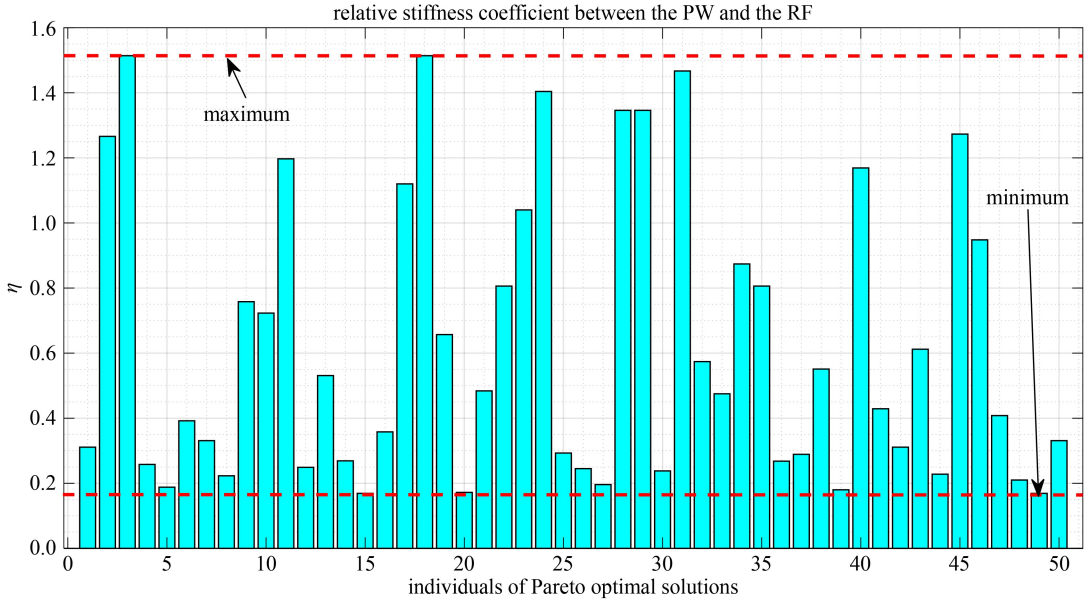

Fig. 6 η of 50 POSs at Generation 50.

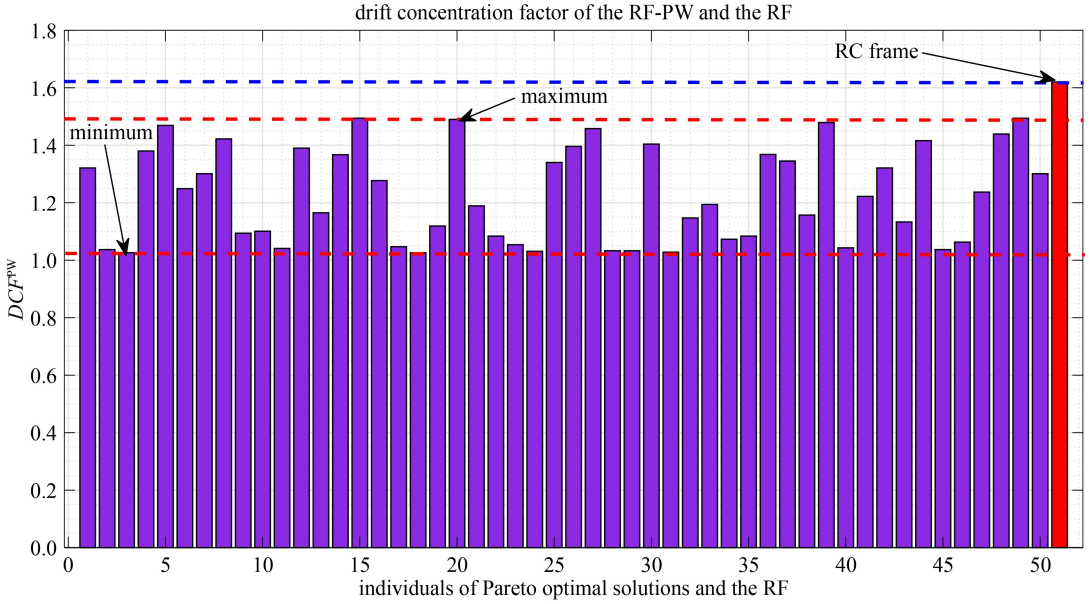

Fig. 7 DCF^{PW} of 50 POSs at Generation 50.

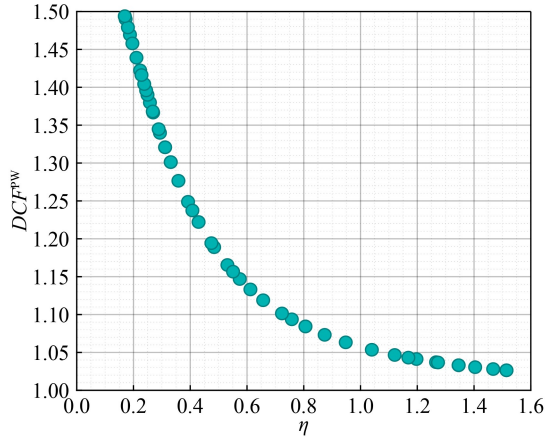

Fig. 8 Trade-off correlation between η and DCF^{PW} at Generation 50.

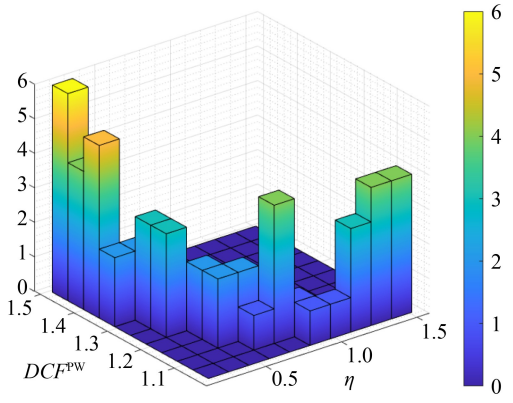

Fig. 9 3D diagram of the quantity distribution of η and DCF^{PW} at Generation 50.

determine the value of b_w.

On the other hand, it is apparent that the distribution of individuals in POSs is also a little biased from Fig. 11. Specifically, more individuals cluster in the end with lower E_wI_w value. In other words, there are more individuals with lower b_w and higher DCF^{PW} in terms of Fig. 14. The reason of this phenomenon may be linked with the constraints of the optimization problem, e.g., due to $1.0 \leqslant DCF^{PW} \leqslant 1.62$, the closer to the lower E_wI_w value the individuals are (i.e., the DCF^{PW} nears to 1.0 and b_w approaches to 8.6 m), the less feasible the design schemes are. For as aforementioned, when the value of DCF closer to 1.0, the corresponding scheme will be impractical due to the demand of the infinite stiffness of the PW. In contrast, when $DCF^{PW} = 1.62$, the scheme corresponds to

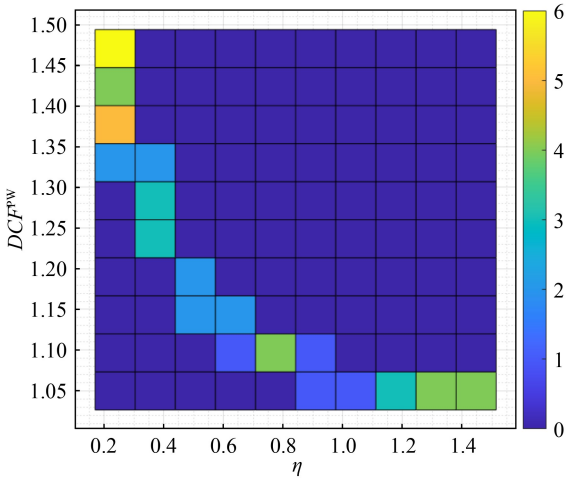

Fig. 10 Plan diagram of the quantity distribution of η and DCF^{PW} at Generation 50.

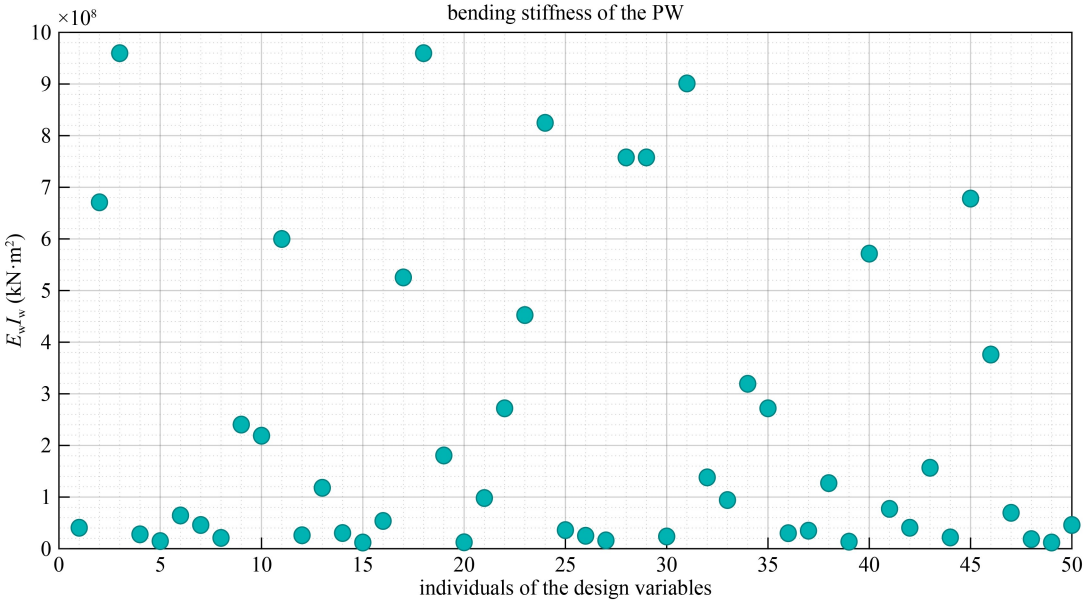

Fig. 11 Scatter diagram of the distribution of E_wI_w at Generation 50.

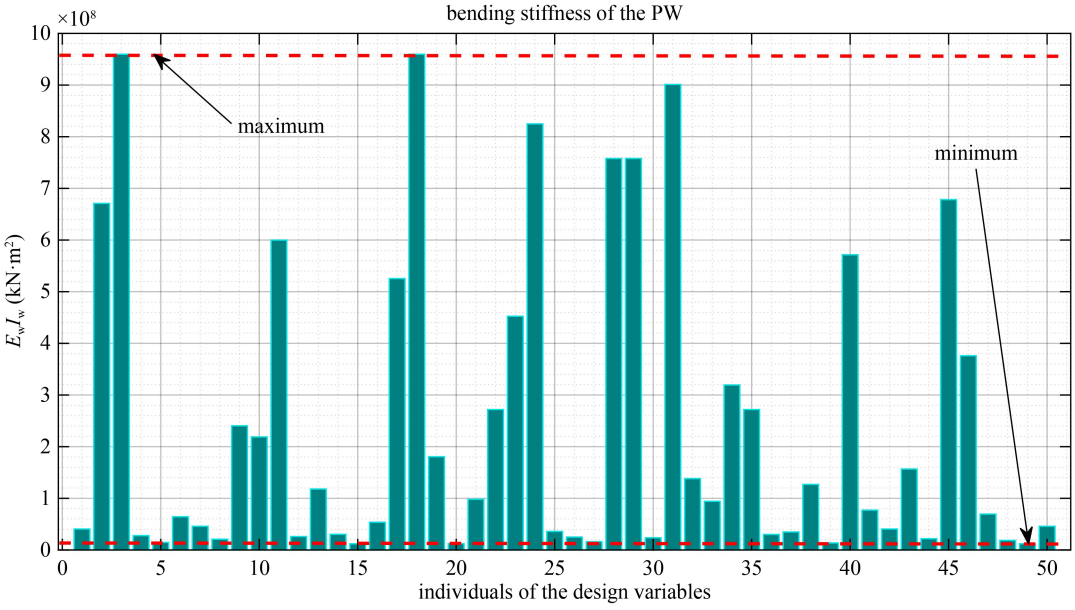

Fig. 12 Bar diagram of the distribution of E_wI_w at Generation 50.

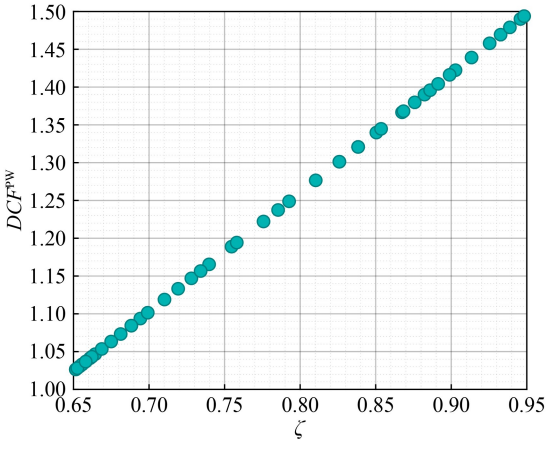

Fig. 13 Correlation between ζ and DCF^{PW} (when t_w = 0.6 m).

the RF, which is an existing structure, i.e., the RF-PW with a value of *DCF* close to 1.62, it needs a lower E_wI_w and easy to be realized. From the perspective of probability, these kinds of solutions have a large probability of occurrence so as to cause the above-mentioned bias phenomenon.

λ has been utilized as a significant parameter in the previous studies on RF-PWs, which is the reciprocal of η as mentioned in Subsection 4.1. For the sake of comparison with the existing findings, the values and diagram of λ are provided in Table 6 and Fig. 15, respectively. As shown in Table 6 and Fig. 15, $0.66 \leqslant \lambda \leqslant 5.905$.

Figures 16 and 17 illustrate the bar diagrams of the distribution of IDR_{max}^{PW} and ζ of 50 POSs at Generation 50, respectively. Figure 18 provides the diagram of the relationship between η and ζ. From Table 6 and Fig. 16, we can know that $\frac{1}{1978} \leqslant IDR_{max}^{PW} \leqslant \frac{1}{1359}$. It is clear that IDR_{max}^{PW} are all less than $IDR_{max}^{RF} = \frac{1}{1289}$ which reflects the effect of the RF after retrofitted by the PW. Furthermore, from Table 6 and Fig. 16, $0.652 \leqslant \zeta \leqslant 0.948$, which means the ratios of IDR_{max}^{PW} over IDR_{max}^{RF} are from 65.2% to 94.8%, respectively.

Moreover, from Fig. 18, it is apparent that the correlation between η and ζ is inverse. That is to say, with the increase of the E_wI_w, the lateral global stiffness of the RF-PW increasingly ascends, so as to lead to the decrease of the IDR_{max}^{PW}.

Figure 19 presents the correlation between ζ and IDR_{max}^{PW}. From Fig. 19, it is apparent that ζ is linearly and positively proportional to IDR_{max}^{PW}, i.e., the larger ζ of the structure is, the bigger the corresponding IDR_{max}^{PW} is, and vice versa. In addition, the values of ζ and IDR_{max}^{PW} are distributed in a reasonable scope, which meets the optimization constraints, such as: $0 < IDR_{max}^{PW} < \frac{1}{1289}$ and $1.0 \leqslant DCF_{max}^{PW} \leqslant 1.62$.

Figures 20 and 21 demonstrate the bar diagrams of the distribution of V_{wb} and δ of 50 POSs at Generation 50, respectively. Figure 22 presents the diagram of the relationship between η and δ. From Table 6 and Fig. 20, we can know that $252.4\ \text{kN} \leqslant V_{wb} \leqslant 723.2\ \text{kN}$, which means the PW shares the lateral load with the RF. Also, From Table 6 and Fig. 21, the ratios of V_{wb} over the resultant force of the lateral load $q \cdot H$, viz. δ are from 15.2% to 43.4%, respectively, which reveals the efficiency provided by the PW to the RF. Furthermore, according to Fig. 22, it is clear that with the increase of η, δ ascends gradually, and vice versa. Meanwhile, when $\eta \leqslant 0.4$, there is an approximately linear relationship

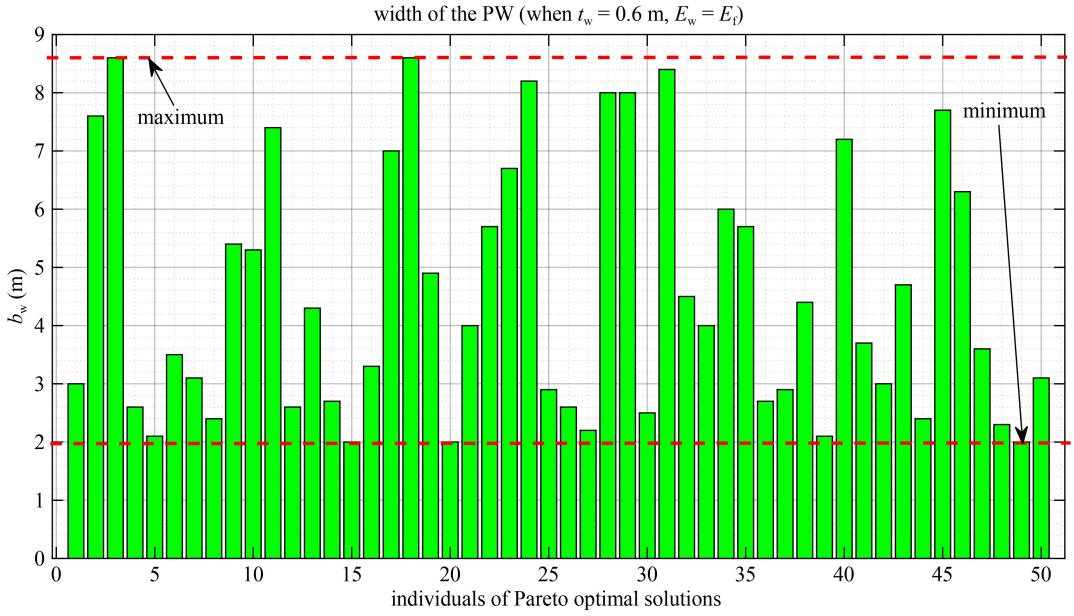

Fig. 14 Bar diagram of the distribution of b_w at Generation 50 (when t_w = 0.6 m).

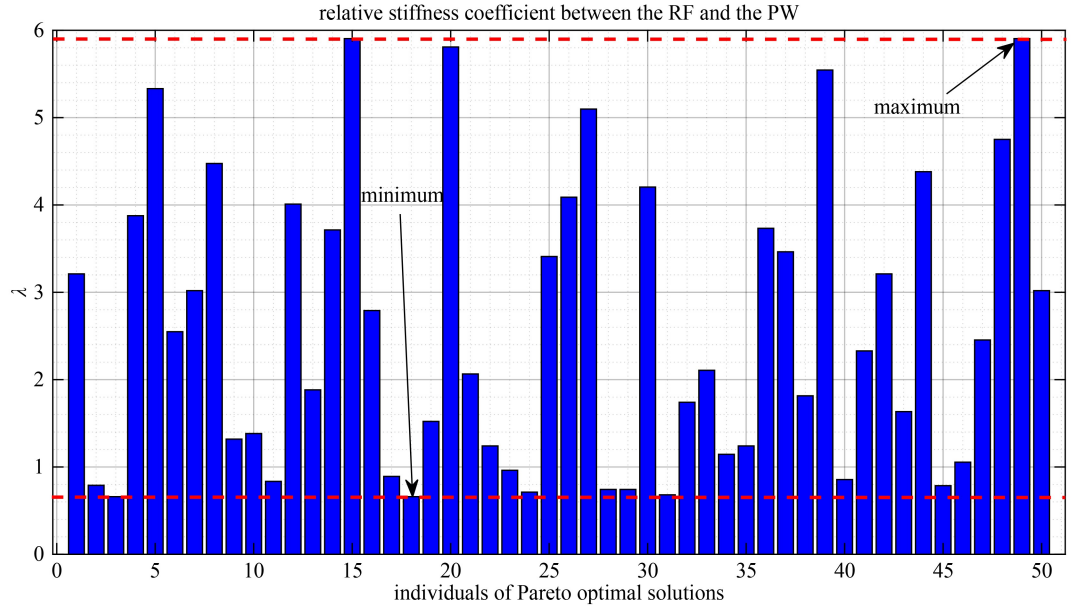

Fig. 15 Bar diagram of the distribution of λ at Generation 50.

between them. By contrast, when $\eta > 0.4$, the growth rate of δ begins to decline gradually and inclines to zero finally, which shows the maximum V_{wb} shared by the PW will not exceed 45% of the resultant force of the lateral load $q \cdot H$ in this case.

Lastly, returning to the aim posed at the beginning of this paper, it is now possible to demonstrate how to apply this multi-objective design method. For instance, (1) if designers want to determine the scheme with the minimum IDR_{max}^{PW}, individual No. 3 would be the best choice on the basis of Table 6. Meantime, other performance indexes relating to individual No. 3 can be found in Table 6 as well; (2) Assuming according to the characteristics of structural plane layout, $b_w = 4.0$ m is suitable to it. As a result, individual No. 21 can be chosen as the best one in the light of Table 6; (3) if a design target value of DCF^{PW} is assigned as 1.320, individual No. 42 would be the second-one choice. The corresponding performance indexes of the 3 chosen individuals can be found in Table 7.

6 Conclusions

The following conclusions can be drawn from the present study.

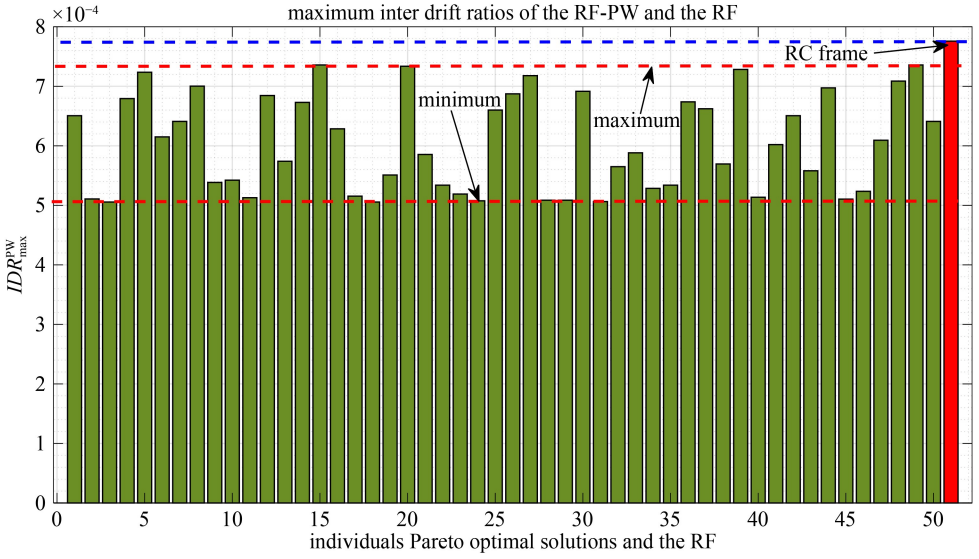

Fig. 16 Bar diagram of the distribution of IDR_{max}^{PW} at Generation 50.

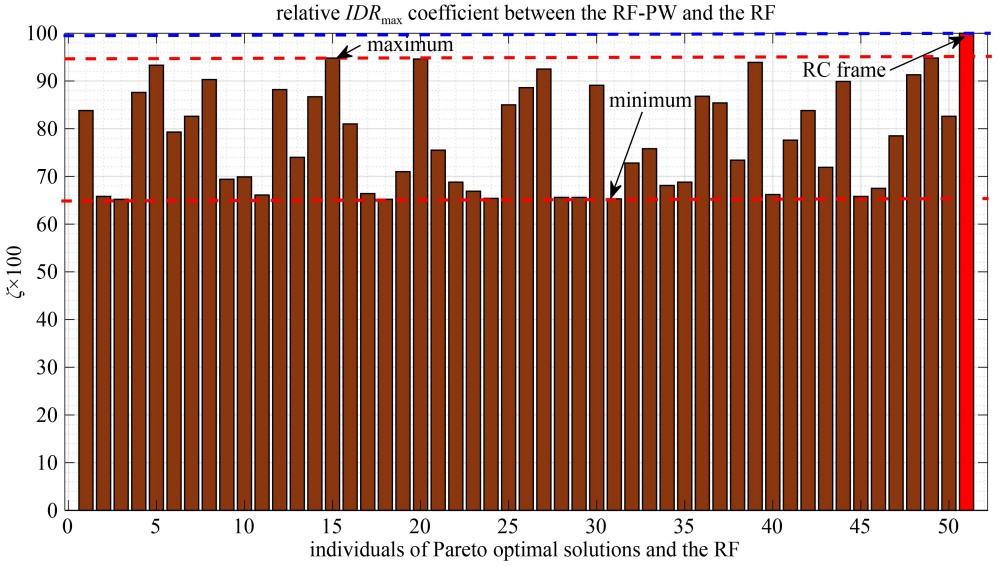

Fig. 17 Bar diagram of the distribution of ζ at Generation 50.

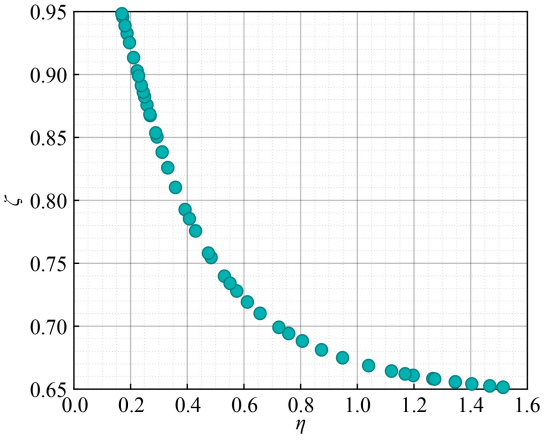

Fig. 18 Correlation between η and ζ.

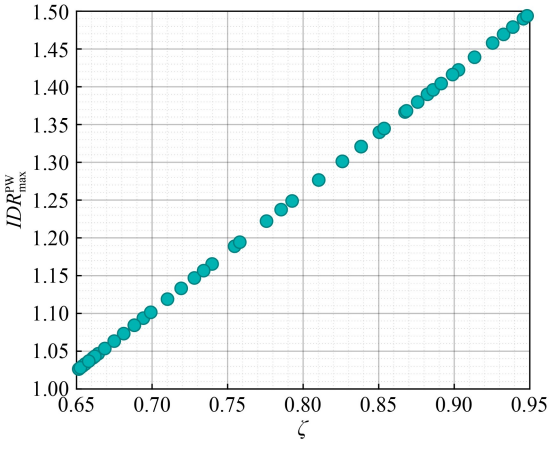

Fig. 19 Correlation between ζ and IDR_{max}^{PW}.

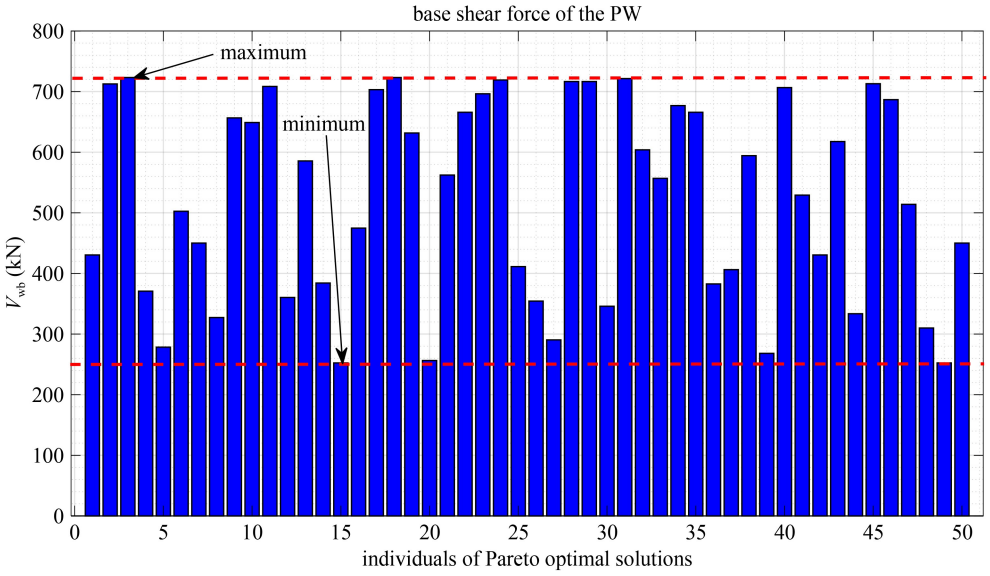

Fig. 20 Bar diagram of the distribution of V_{wb} at Generation 50.

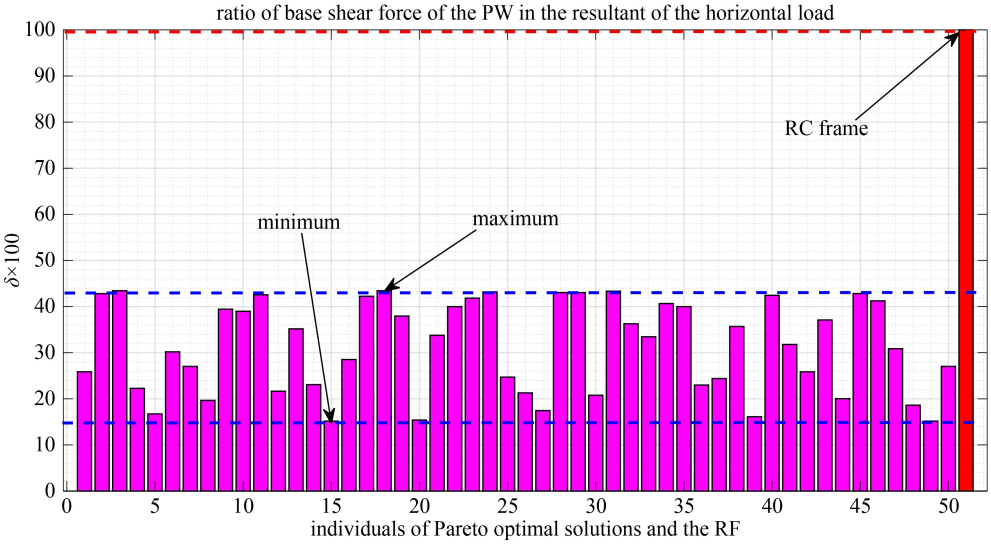

Fig. 21 Bar diagram of the distribution of δ at Generation 50.

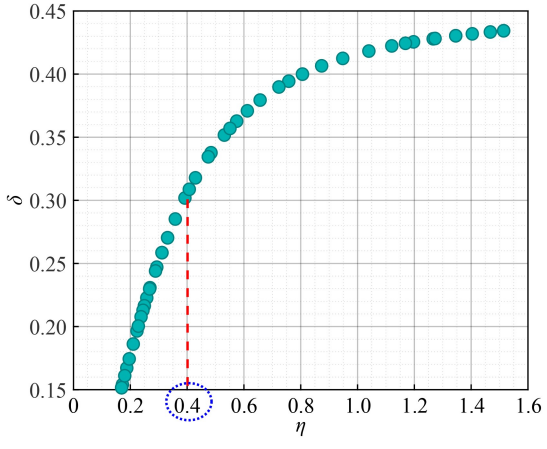

Fig. 22 Correlation between η and δ.

1) A multi-objective design method has been developed for seismic retrofitting of existing RFs using PWs. Then, it has been investigated and verified via a real structure. The results demonstrated that this method is feasible, practical and can be employed for the preliminary design of these kinds of structures.

2) MEO is integrated to produce POSs with a certain number of structural performance indexes. After that, the most suitable one can be picked out based on the requirements of practical projects so that the blindness in determining the target value of *DCF* can be addressed.

3) Owing to POSs, designers can compare and weigh the pros and cons of them, a best one can be determined so that the idea of performance-based design can be realized through this method.

Limitation and future studies:

Table 7 Performance indexes of the 3 chosen individuals

No.	η	DCF^{PW}	$E_wI_w \times 10^{-7}$ (kN·m^2)	b_w (m) / t_w = 0.6 m	λ	IDR_{max}^{PW}	ζ	V_{wb} (kN)	δ
3	1.514	1.026	96.0	8.6	0.660	1/1978	65.2%	723.2	43.4%
21	0.484	1.189	9.812	4.0	2.065	1/1708	75.5%	562.3	33.8%
42	0.311	1.321	4.058	3.0	3.211	1/1537	83.8%	430.5	25.9%

1) In this paper, the research about the proposed design procedure of PWs as retrofitting system is based on elastic theory. The nonlinear seismic analysis are necessary to investigate the actual behavior of the RF-PWs.

2) The effects of the high modes are getting obvious with the increase of structure height. Therefore, the effects of the high modes should be considered when analyzing the structural performance.

Acknowledgements The authors are grateful for the financial supports from the Scientific Research Fund of Institute of Engineering Mechanics, China Earthquake Administration (Nos. 2019D12 and 2019D11); Open Foundation of State Key Laboratory of Disaster Reduction in Civil Engineering, Tongji University in China (No. SLDRCE19-01); Foundation of Public Welfare Technology Research Project of Zhejiang Province in China (No. LGF20E080013); Natural Science Foundation of Zhejiang Province, China (No. LY22E080003); Fundamental Research Fund for the Provincial Universities of Zhejiang (No. SJLZ2022003) and Foundation of Public Welfare Technology Research Project of Ningbo in China, (Nos. 2022S170, 2022S179).

References

1. Qu Z, Wada A, Motoyui S, Sakata H, Kishiki S. Pin-supported walls for enhancing the seismic performance of building structures. Earthquake Engineering & Structural Dynamics, 2012, 41(14): 2075−2091
2. Fabio M. A simplified retrofitting method based on seismic damage of a SDOF system equivalent to a damped braced building. Engineering Structures, 2019, 200: 109512
3. Mehrdad A, Nicos M. Seismic response of a yielding structure coupled with a rocking wall. Journal of Structural Engineering, 2017, 144(2): 4017196
4. Barbagallo F, Bosco M, Marino E M, Rossi P P, Stramondo P R. A multi-performance design method for seismic upgrading of existing RC frames by BRBs. Earthquake Engineering & Structural Dynamics, 2017, 46(7): 1099−1119
5. Di Sarno L, Manfredi G. Seismic retrofitting with buckling restrained braces: Application to an existing non-ductile RC framed building. Soil Dynamics and Earthquake Engineering, 2010, 30(11): 1279−1297
6. Di Sarno L, Manfredi G. Experimental tests on full-scale RC unretrofitted frame and retrofitted with buckling-restrained braces. Earthquake Engineering & Structural Dynamics, 2012, 41(2): 315−333
7. Sutcu Fatih, Takeuchi T, Matsui R. Seismic retrofit design method for RC buildings using buckling-restrained braces and steel frames. Journal of Constructional Steel Research, 2014, 101: 304−313
8. Almeida A, Ferreira R, Proença J M, Gago A S. Seismic retrofit of RC building structures with Buckling Restrained Braces. Engineering Structures, 2017, 130: 14−22
9. Saingam P, Sutcu F, Terazawa Y, Fujishita K, Lin P C, Celik O C, Takeuchi T. Composite behavior in RC buildings retrofitted using buckling-restrained braces with elastic steel frames. Engineering Structures, 2020, 219: 110896
10. Dalalbashi A, Eslami A, Ronagh H R. Plastic hinge relocation in RC joints as an alternative method of retrofitting using FRP. Composite Structures, 2012, 94(8): 2433−2439
11. Marletta M, Caliò I. Seismic resistance of a reinforced concrete building before and after retrofitting Part I: The existing building. Structures under Shock and Impact, 2004, 8: 293−304
12. Marletta M, Vaccaro S, Caliò I. Seismic resistance of a reinforced concrete building before and after retrofitting Part II: The retrofitted building. Structures under Shock and Impact, 2004, 8: 307−322
13. Han R, Yue L, Van De Lindt J. Probabilistic assessment and cost-benefit analysis of nonductile reinforced concrete buildings retrofitted with base isolation: considering mainshock–aftershock hazards. ASCE-ASME Journal of Risk and Uncertainty Engineering Systems, Part A. Civil Engineering (New York, N.Y.), 2017, 3(4): 4017023
14. De Luca A, Mele E, Molina J, Verzeletti G, Pinto A V. Base isolation for retrofitting historic buildings: Evaluation of seismic performance through experimental investigation. Earthquake Engineering & Structural Dynamics, 2001, 30(8): 1125−1145
15. Mazza F, Mazza M, Vulcano A. Nonlinear response of R.C. framed buildings retrofitted by different base-isolation systems under horizontal and vertical components of near-fault earthquakes. Earthquakes and Structures, 2017, 12(1): 135−144
16. Mazza F, Mazza M, Vulcano A. Base-isolation systems for the seismic retrofitting of R. C. framed buildings with soft-storey subjected to near-fault earthquakes. Soil Dynamics and Earthquake Engineering, 2018, 109: 209−221
17. Mazza F, Pucci D. Static vulnerability of an existing R. C. structure and seismic retrofitting by CFRP and base-isolation: A case study. Soil Dynamics and Earthquake Engineering, 2016, 84: 1−12
18. Smith J W, Sullivan T J, Nascimbene R. Precast concrete spreader-walls to improve the reparability of RC frame buildings. Earthquake Engineering & Structural Dynamics, 2021, 50(3): 831−844
19. Fabio M. Dissipative steel exoskeletons for the seismic control of reinforced concrete framed buildings. Structural Control and

Health Monitoring, 2021, 28(3): e2683
20. Barbagallo F, Bosco M, Marino E M, Rossi P P. Seismic retrofitting of braced frame buildings by RC rocking walls and viscous dampers. Earthquake Engineering & Structural Dynamics, 2018, 47(13): 2682−2707
21. Wada A, Qu Z, Motoyui S, Sakata H. Seismic retrofit of existing SRC frames using rocking walls and steel dampers. Frontiers of Architecture and Civil Engineering in China, 2011, 5(3): 259−266
22. Marriott D J, Pampanin S, Bull D K, Palermo A. Improving the seismic performance of existing reinforced concrete buildings using advanced rocking wall solutions. In: NZSEE Annual Technical Conference. 2007
23. Eldin M N, Dereje A J, Kim J. Seismic retrofit of framed buildings using self-centering PC frames. Journal of Structural Engineering, 2020, 146(10): 04020208
24. Zibaei H, Mokari J. Evaluation of seismic behavior improvement in RC MRFs retrofitted by controlled rocking wall systems. Structural Design of Tall and Special Buildings, 2014, 23(13): 995−1006
25. Alavi B, Krawinkler H. Strengthening of moment-resisting frame structures against near-fault ground motion effects. Earthquake Engineering & Structural Dynamics, 2004, 33(6): 707−722
26. Ying Z, Yao D, Yue C. Li, Qingqian. Upgraded parameter model of frame pin-supported wall structures. Structural Design of Tall and Special Buildings, 2021, 30(8): e1852
27. Sun T, Kurama Y C, Ou J. Practical displacement-based seismic design approach for PWF structures with supplemental yielding dissipators. Engineering Structures, 2018, 172: 538−553
28. Konak A, Coit D W, Smith A E. Multi-objective optimization using genetic algorithms: A tutorial. Reliability Engineering & System Safety, 2006, 91(9): 992−1007
29. Chen Y, Zhang Z. Analysis of outrigger numbers and locations in outrigger braced structures using a multiobjective genetic algorithm. Structural Design of Tall and Special Buildings, 2018, 27(1): e1408
30. Chen Y, Cai K, Wang X. Parameter study of framed-tube structures with outriggers using genetic algorithm. Structural Design of Tall and Special Buildings, 2018, 27(14): e1499
31. Chisari C, Bedon C. Performance-based design of FRP retrofitting of existing RC frames by means of multi-objective optimisation. Bollettino di Geofisica Teorica ed Applicata, 2017, 58(4): 377−394
32. Deb K, Pratap A, Agarwal S, Meyarivan T. A fast and elitist multiobjective genetic algorithm: NSGA-II. IEEE Transactions on Evolutionary Computation, 2002, 6(2): 182−197
33. Andrey P. Genetic Algorithm Optimization Toolbox, User's Guide. MathWorks, Inc., 2011
34. Pan P, Wu S, Nie X. A distributed parameter model of a frame pin-supported wall structure. Earthquake Engineering & Structural Dynamics, 2015, 44(10): 1643−1659
35. Wu D, Zhao B, Lu X. Dynamic behavior of upgraded rocking wall-moment frames using an extended coupled-two-beam model. Soil Dynamics and Earthquake Engineering, 2018, 115: 365−377